Parity-Violating Inelastic Electron-Proton Scattering at Low Q^2

D. Androić,[1] D.S. Armstrong,[2] A. Asaturyan,[3] J. Balewski,[4] K. Bartlett,[2] J. Beaufait,[5] R.S. Beminiwattha,[6] J. Benesch,[5] F. Benmokhtar,[7] J. Birchall,[8] R.D. Carlini,[5,2] J.C. Cornejo,[2] S. Covrig Dusa,[5] M.M. Dalton,[9,5] C.A. Davis,[10] W. Deconinck,[2] J. Diefenbach,[11] J.F. Dowd,[2] J.A. Dunne,[12] D. Dutta,[12] W.S. Duvall,[13] M. Elaasar,[14] W.R. Falk,[8,*] J.M. Finn,[2,*] T. Forest,[15,16] C. Gal,[9] D. Gaskell,[5] M.T.W. Gericke,[8] J. Grames,[5] V.M. Gray,[2] K. Grimm,[16,2] F. Guo,[4] J.R. Hoskins,[2] D. Jones,[9] M.K. Jones,[5] R. Jones,[17] M. Kargiantoulakis,[9] P.M. King,[6] E. Korkmaz,[18] S. Kowalski,[4] J. Leacock,[13] J. Leckey,[2] A.R. Lee,[13] J.H. Lee,[2,6] L. Lee,[10,8] S. MacEwan,[8] D. Mack,[5] J.A. Magee,[2,19] R. Mahurin,[8] J. Mammei,[13,8] J.W. Martin,[20] M.J. McHugh,[21] D. Meekins,[5] J. Mei,[5] K.E. Mesick,[21,22] R. Michaels,[5] A. Micherdzinska,[21] A. Mkrtchyan,[3] H. Mkrtchyan,[3] N. Morgan,[13] A. Narayan,[12] L.Z. Ndukum,[12] V. Nelyubin,[9] H. Nuhait,[16] Nuruzzaman,[11,12] W.T.H van Oers,[10,8] V.F. Owen,[2] S.A. Page,[8] J. Pan,[8] K.D. Paschke,[9] S.K. Phillips,[23] M.L. Pitt,[13] M. Poelker,[5] R.W. Radloff,[6] J.F. Rajotte,[4] W.D. Ramsay,[10,8] J. Roche,[6] B. Sawatzky,[5] T. Seva,[24] M.H. Shabestari,[12] R. Silwal,[9] N. Simicevic,[16] G.R. Smith,[5] P. Solvignon,[5,*] D.T. Spayde,[25] A. Subedi,[12] R. Subedi,[21] R. Suleiman,[5] V. Tadevosyan,[3] W.A. Tobias,[9] V. Tvaskis,[20,8] B. Waidyawansa,[6] P. Wang,[8] S.P. Wells,[16] S.A. Wood,[5] S. Yang,[2] R.D. Young,[26] P. Zang,[27] and S. Zhamkochyan[3]

($Q_{\rm weak}$ Collaboration)

[1] *University of Zagreb, Zagreb, HR 10002 Croatia*
[2] *College of William and Mary, Williamsburg, VA 23185, USA*
[3] *A. I. Alikhanyan National Science Laboratory (Yerevan Physics Institute), Yerevan 0036, Armenia*
[4] *Massachusetts Institute of Technology, Cambridge, MA 02139, USA*
[5] *Thomas Jefferson National Accelerator Facility, Newport News, VA 23606, USA*
[6] *Ohio University, Athens, OH 45701, USA*
[7] *Christopher Newport University, Newport News, VA 23606, USA*
[8] *University of Manitoba, Winnipeg, MB R3T2N2, Canada*
[9] *University of Virginia, Charlottesville, VA 22903, USA*
[10] *TRIUMF, Vancouver, BC V6T2A3, Canada*
[11] *Hampton University, Hampton, VA 23668, USA*
[12] *Mississippi State University, Mississippi State, MS 39762, USA*
[13] *Virginia Polytechnic Institute & State University, Blacksburg, VA 24061, USA*
[14] *Southern University at New Orleans, New Orleans, LA 70126, USA*
[15] *Idaho State University, Pocatello, ID 83209, USA*
[16] *Louisiana Tech University, Ruston, LA 71272, USA*
[17] *University of Connecticut, Storrs-Mansfield, CT 06269, USA*
[18] *University of Northern British Columbia, Prince George, BC V2N4Z9, Canada*
[19] *Lawrence Livermore National Laboratory, Livermore, CA 94550, USA*
[20] *University of Winnipeg, Winnipeg, MB R3B2E9, Canada*
[21] *George Washington University, Washington, DC 20052, USA*
[22] *Rutgers, the State University of New Jersey, Piscataway, NJ 08854, USA*
[23] *University of New Hampshire, Durham, NH 03824, USA*
[24] *University of Zagreb, Zagreb, HR 10002, Croatia*
[25] *Hendrix College, Conway, AR 72032, USA*
[26] *University of Adelaide, Adelaide, SA 5005, Australia*
[27] *Syracuse University, Syracuse, New York 13244, USA*

(Dated: July 1, 2019)

The parity-violating asymmetry was measured for the inelastic scattering of electrons from the proton, at $Q^2 = 0.082$ GeV^2 and $W = 2.23$ GeV, above the resonance region. The result $A_{\rm inel} = -13.5 \pm 2.0({\rm stat}) \pm 3.9({\rm syst})$ ppm is in agreement with theoretical calculations, and helps to validate the modeling of the γZ interference structure functions $F_1^{\gamma Z}$ and $F_2^{\gamma Z}$ used in those calculations, which are also used for determination of the $\Box_{\gamma Z}$ contribution to parity-violating elastic scattering measurements. A positive parity-violating asymmetry for inclusive π^- production was observed, as well as positive beam-normal single spin asymmetry for scattered electrons and a negative beam-normal single spin asymmetry for inclusive π^- production.

* Deceased

I. MOTIVATION

The importance of two-boson exchange processes (e.g., $\gamma\gamma, \gamma Z$) to precision electromagnetic and electroweak physics has become increasingly apparent in recent years. For example, it is now widely believed that two-photon exchange contributions can explain much (perhaps all) of the striking difference in the proton form factor ratio G_E^p/G_M^p as extracted from cross sections using the Rosenbluth separation technique and that obtained from recoil polarization measurements, e.g., [1] (see [2] for a recent review). Two-photon box diagrams generate such observables in electron scattering as beam-normal single spin asymmetries [3] and target-normal single-spin asymmetries [4], as well as differences between e^-p and e^+p scattering cross sections [5, 6], all of which have motivated a number of experiments [7–17]. Superallowed nuclear beta-decay measurements, which are critical ingredients to tests of the unitarity of the CKM matrix, have γW and WZ box diagrams as their largest nucleus-independent radiative corrections [18], and so theoretical control of these diagrams is therefore highly desirable [19].

A particular example of the relevance of two-boson exchange diagrams is the case of the γZ box diagram in parity-violating electron scattering (PVES). In PVES, longitudinally-polarized electrons scatter from an unpolarized target (a proton in the present case), and electroweak interference generates an asymmetry between the scattering cross section for right-handed (σ_R) and left-handed (σ_L) electrons,

$$A_{\rm PV} = \frac{\sigma_R - \sigma_L}{\sigma_R + \sigma_L}$$

Elastic PVES on the proton has been used as a powerful low-energy test of the Standard Model [20], because at sufficiently small four-momentum transfer Q^2, and for forward-angle scattering, this asymmetry depends in a simple way on the proton's weak charge, Q_W^p, via

$$A_{PV}/A_0 = Q_W^p + Q^2 B(Q^2, \theta), \quad A_0 = \left[\frac{-G_F Q^2}{4\pi\alpha\sqrt{2}}\right]. \tag{1}$$

where G_F the Fermi constant, α is the fine structure constant, $-Q^2$ is the four-momentum transfer squared, and $B(Q^2)$ encodes hadron structure effects. Within the framework of the Standard Model, the weak charge depends in turn on the weak mixing angle, $\sin^2\theta_W$, through the tree-level relation $Q_W^p = 1 - 4\sin^2\theta_W$.

Including radiative corrections, we have [21]:

$$Q_W^p = (\rho + \Delta_e)\left(1 - 4\sin^2\theta_W(0) + \Delta_e'\right) + \Box_{WW} + \Box_{ZZ} + \Box_{\gamma Z}(0). \tag{2}$$

where $\sin^2\theta_W(0)$ is the weak mixing angle at zero momentum transfer. The electroweak radiative correction terms ρ, Δ_e, and Δ_e' are under good theoretical control and have been calculated to sufficient precision [21] for interpretation of existing [20] and planned [22] measurements of the weak charge. Similarly, the box diagram terms $\Box_{WW}$ and $\Box_{ZZ}$, which are amenable to evaluation via pQCD, are known to adequate precision [23]. Thus the weak charge Q_w^p is well-predicted within the Standard Model and provides an excellent low-energy avenue to search for new physics, motivating the recent $\rm Q_{weak}$ [20] and future P2 [22] experiments.

This satisfactory situation was upset when Gorchtein and Horowitz [24] revealed that the γZ box diagram $\Box_{\gamma Z}$ (in particular, the term $\Box_{\gamma Z}^V$, the piece which involves the axial electron current and the vector hadron current) was both strongly energy-dependent and much larger (at the relevant beam energy scale) than had been claimed in earlier estimates. Of critical importance, they showed that the uncertainty on $\Box_{\gamma Z}^V$ was large enough to add significantly to the uncertainty aimed for by experiment.

Following on that initial work by Gorchtein and Horowitz, several different theoretical groups have performed calculations of the $\Box_{\gamma Z}^V$ term. Gratifyingly, there is excellent agreement on the size of $\Box_{\gamma Z}^V$ from all these calculations [25–31], although there is not yet consensus on the size of the theoretical uncertainty on $\Box_{\gamma Z}^V$.

The most important input to these calculations are the γZ interference structure functions $F_1^{\gamma Z}$ and $F_2^{\gamma Z}$, which are functions of Q^2 and W^2 (or, equivalently, Q^2 and Bjorken x). Unfortunately, experimental input on these structure functions is scarce, unlike their pure electromagnetic analogs F_1^γ and F_2^γ. While there have been extractions of $F_1^{\gamma Z}$ and $F_2^{\gamma Z}$ using neutral current deep inelastic scattering (DIS) experiments at HERA [32], those data were at very high Q^2 (> 60 GeV^2) and small Bjorken x, while the region of the dispersion integral that is important for $\Box_{\gamma Z}^V$ calculation is high x and low Q^2. The various $\Box_{\gamma Z}^V$ calculations differ primarily in how they choose to model $F_1^{\gamma Z}$ and $F_2^{\gamma Z}$ in this kinematic regime, and in the uncertainties ascribed to this modeling.

This modeling of the γZ interference structure functions can be tested by comparing to parity-violating electron scattering data. However, there are only two previous PVES experiments that can be used to constrain or test models

of $F_1^{\gamma Z}$ and $F_2^{\gamma Z}$. These are the measurement of parity-violating inelastic scattering near the $\Delta(1232)$ resonance by the G0 collaboration, who extracted the parity-violating asymmetry from the proton and deuteron at $Q^2 = 0.34$ GeV^2 and $W = 1.18$ GeV [33], and the JLab Hall A E08-011 (PVDIS) collaboration, which measured asymmetries from electron-deuteron scattering over several values of W between 1.2 to 1.98 GeV and Q^2 between 0.95 and 1.47 GeV^2 [34]. Constraints based on the results from these two experiments were applied by the Adelaide-Manitoba-Jefferson Lab (AJM) theoretical group [30] and were important in reducing their quoted uncertainty in $\Box_{\gamma Z}^V$. The AJM group subsequently applied quark-hadron duality parton distribution function (PDF) fits in order to apply additional constraints on the interference structure functions [31].

Additional experimental input to test these models of the interference structure functions, and thus test the calculation of the $\Box_{\gamma Z}^V$ diagram, would clearly be valuable; this motivated the present measurement. During a special running period of the Q_{weak} experiment, the beam energy was raised in order for us to measure the parity-violating asymmetry from the proton in an inelastic region of interest ($Q^2 = 0.082$ GeV^2 and $W = 2.23$ GeV) for the $\Box_{\gamma Z}^V$ calculations, and for which asymmetry predictions were available using the structure function models from two of the theoretical groups (AJM [30] and Gorchtein *et al.* [26]). In the remainder of this paper we describe this measurement and the data analysis, and compare the extracted asymmetry to the model predictions.

II. EXPERIMENT

The measurement was conducted using the Q_{weak} apparatus which was located in Hall C at the Thomas Jefferson National Accelerator Facility. This apparatus was optimized for the measurement of the parity-violating asymmetry in the elastic scattering of longitudinally-polarized electrons at a 1.16 GeV beam energy from the protons in a liquid hydrogen target (the Q_{weak} weak charge measurement [20]). A detailed discussion of the apparatus is available elsewhere [35]; here we provide an overview, followed by a presentation of those aspects that were modified for the present measurement.

The Q_{weak} apparatus was designed to detect electrons scattered from the target with scattering angles between 5.8° and 11.6° (polar) and 49% of 2π in azimuth. The angular acceptance was defined by a series of three sets of precision lead-alloy collimators, each set with eight symmetric apertures in θ and ϕ. The azimuthal acceptances were matched to the eight open sectors ("octants") of the toroidal spectrometer magnet. Momentum-selected scattered electrons were detected by one of eight identical fused-silica Cherenkov detectors, in an azimuthally-symmetric array, one detector per magnet octant. These detectors, called our main detectors (MD, numbered MD1 to MD8) were rectangular bars, 2 m in length, 18 cm in width and 1.25 cm in thickness. Cherenkov light was read out from each MD using a pair of photomultiplier tubes (PMTs), one located at each end of a given detector. Just upstream of each MD was located a 2-cm thick Pb pre-radiator, which served to amplify the signal from incident electrons through generation of an electromagnetic shower and also to suppress low-energy backgrounds. The main detectors were enclosed in a concrete shielding hut, with 122 cm thick walls. The upstream face of the hut was constructed of 80 cm thick high-density (2700 kg/m^3) barite-loaded concrete (Ba_2SO_4).

In the standard mode of data-taking used for the asymmetry measurements, the current produced by each main detector PMT was converted to a voltage and integrated during ~ 1 ms long periods, known as "windows", during which the electron beam helicity was held constant (see below). The integrated PMT signal for each helicity window was then digitized and recorded. This mode of data-taking is referred to here as "Integrating Mode".

An alternate mode, known as "Event Mode", was used in which the beam current was reduced substantially (to ~ 0.1 nA), and PMT signals caused by individual scattering events were read out individually and digitized in a conventional manner. This enabled pulse-height and timing analysis of individual scattered events, which was useful for determining background fractions. During Event Mode data taking, a set of drift chambers, known as the the tracking system, were inserted upstream and downstream of the magnet to track individual charged particles during dedicated periods of low-current running. This system was used for calibration purposes, background studies, and for confirmation of the kinematics and acceptance of the detected electrons.

The polarized electron beam's helicity was selected 960 times per second, allowing the beam to be produced in a sequence of "helicity quartets", either $(+--+)$ or $(-++-)$, with the pattern chosen pseudorandomly at 240 Hz. The quartet pattern served to cancel effects due to slow linear drifts in beam properties or detector gains, while the rapid helicity reversal suppressed noise contributions due to fluctuations in either the target density or beam properties. An additional "slow" reversal of the helicity was done every 4 hours by insertion or removal of a half-wave plate in the path of the circularly-polarized laser beam used to generate the polarized electron beam. A third, independent reversal method, using a "double Wien" electron-spin rotator [36] in the accelerator's injector region, which was developed for the primary Q_{weak} experiment, was not used during the present short measurement.

Continuous measurements of the incident electron beam current were made using three independent radio-frequency resonant-cavity beam current monitors (BCM), the beam trajectory was measured using five beam position monitors

(BPM), located upstream of the target, and energy changes were measured using another BPM at a dispersive location in the beam line.

The primary target was a high-power cryogenic liquid hydrogen target. The hydrogen was maintained at 20 K and was contained in an aluminum-walled target cell, 34.4 cm in length, with thin Al-alloy entrance and exit windows (respectively, 0.11 mm and 0.13 mm thick). Several additional solid targets were available, in particular a 3.7 mm thick Al target, made with the same alloy as the hydrogen target entrance and exit windows; the thickness of the Al target was chosen to match the radiation length of the hydrogen target.

For the present measurement, the apparatus and experimental conditions were modified in several ways. The beam energy was raised to 3.35 GeV, in order to access the inelastic scattering kinematics of interest; the incident beam current was maintained between 160 and 180 μA. Due to beam-delivery requirements for an experiment running concurrently in another experimental hall, it was not possible to deliver an electron beam which was polarized fully in the longitudinal direction. Instead, the electron spin angle during the "production" data set was at $\theta_P^{\rm prod} = -19.7^\circ \pm 1.9^\circ$, where a positive angle corresponds to an angle measured from the beam axis ($+z$-axis), rotated towards beam right ($+x$-axis). This corresponded to an electron spin with a 94.1% longitudinal component and a 33.7% (horizontal) transverse component. Beam of the same energy, but polarized almost entirely in the horizontal transverse orientation, with a polarization angle of $\theta_P^{\rm trans} = 92.2^\circ \pm 1.9^\circ$, was available for part of the data-taking, which we refer to as the "transverse" data set.

The overall magnitude of the polarization of the electron beam was $(P = 87.0 \pm 0.6)\%$ for both production and transverse data, as periodically measured by the Moller polarimeter [37] in Hall C.

Due to the higher beam energy, a significant background was present in the main detectors caused by negative pions produced in the target with similar momenta to the inelastically scattered electrons of interest. Positively charged pions were swept out of the acceptance by the spectrometer magnetic field. With the high-rate integrating mode of detector readout, it is not possible to separate the contributions of individual electrons from individual pions to the asymmetry measurement. In order to measure and correct for this pion background, one of the main detectors (in octant 7) was modified so as to have an enhanced sensitivity to pions. The modification was the addition of a 10.2 cm thick Pb absorber (~ 18 radiation lengths), placed just upstream of the detector, which significantly attenuated the signal in this detector from scattered electrons, while allowing the majority of the ~ 1 GeV pions to generate signals. Thus the asymmetry in MD7 was dominated by that from incident pions, with a different mixture of electron and pion signals than that for the other 7 main detectors. Under the assumption that the pion and electron fluxes were azimuthally symmetric, this difference allowed an unfolding of the separate electron and pion asymmetries. We refer to the detectors other than MD7 as "unblocked" detectors.

The production data set on the hydrogen target included 9.4×10^7 helicity quartets (108 hours of data-taking), and the transverse data set included 3.7×10^6 helicity quartets (4.3 hours of data-taking). The rate of charged particles incident on each unblocked detector was approximately 9 MHz, of which approximately 27% were pions and 73% electrons. As a typical electron produced significantly more light in a main detector than did a pion, the fraction of the integrated detector signal due to pions (see below) was 9.6%, with the remainder being mainly due to electrons.

In order to measure the asymmetry caused by electrons scattering from the target entrance and exit windows, production data were also taken on the Al alloy target; for these runs the beam current was reduced to 60 μA. This aluminum data set included 5.2×10^6 helicity quartets (6.0 hours of data-taking).

III. DATA ANALYSIS

The extraction of the parity-violating asymmetry for the inelastic scattering events took place in several steps. Event Mode data were used to determine the fraction of the experimental yield that arose due to pions and neutral particles (Sec. III A). The Integrating Mode data were used to form asymmetries for each detector, and these were then corrected for several classes of false asymmetry (Sec. III B). The resulting asymmetries and yield fractions for all eight detectors were analyzed in a combined fit in order to separately extract the transverse and longitudinal asymmetries for both electrons and pions (Sec. III C). Finally, the longitudinal electron asymmetry A_e^L obtained from this fit was corrected for the effect of various backgrounds (Sec. III D) in order to obtain the inelastic parity-violating asymmetry $A_{\rm inel}$.

Each of these steps in the analysis is described in the following sections. Further details can be found in the PhD thesis of one of us [38].

A. Yield Fraction Determination

Event Mode data were used to determine the fraction of the yield in the detectors that were caused by pions (as opposed to the desired electrons) and by neutral particles. The existence of the Pb wall in front of the "blocked" detector (MD7) meant that these determinations were done differently for that detector compared to the seven other unblocked detectors, as discussed below.

1. *Pion yield fraction in unblocked detectors*

Event Mode data were used to determine f_π, the fraction of the signal seen in the detectors that was due to pions (or muons from their decay; these were treated together, and henceforth "pions" will refer to both). We note that negative pions can only arise in electron scattering on hydrogen through multi-pion production processes. There is a paucity of multi-pion production cross-section data available in the relevant kinematic range for this experiment, and so we relied on measured pulse-height distributions in the main detectors to determine f_π. Figure 1 shows a typical pulse-height spectrum for an unblocked main detector, obtained during Event Mode data-taking. The spectrum is a sum of the signals of the two PMTs that read out the detector, and the electronic pedestal has been subtracted. The peak at larger amplitude due to the showering electrons is clearly seen, along with the peak at lower amplitude due to the (minimum-ionizing) pions.

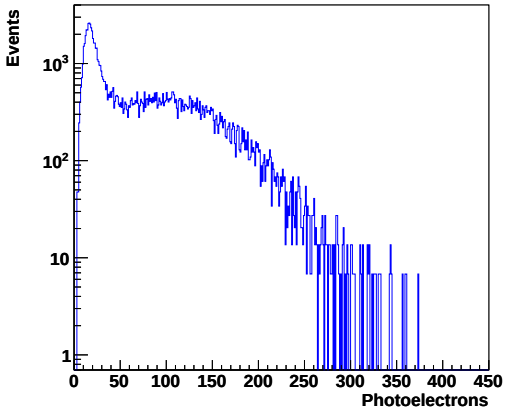

FIG. 1. Typical photoelectron spectrum, after subtraction of the electronic pedestal, for an unblocked main detector (MD4). Two distinct peaks can be see. The narrow peak on the left, centered near 20 photoelectrons, is due to pions. The broader peak on the right, centered near 100 photoelectrons, is due to electrons.

In order to fit these spectra to determine the fractional signal from pions and electrons, separate GEANT4 [39] simulations were generated of electrons and pions, of appropriate momenta, incident on a detector, with the generation and tracking of optical photons enabled in the simulation. These simulations provided pulse-height distributions for the two particle types. The experimental pulse-height spectra for each of the unblocked main detectors were fitted to a linear combination of the simulated pion and electron spectra, with the relative fractions of the two particle types as a free parameter. The fit also included a scaling factor between photoelectrons (simulation) and electronic channels (data), one factor for each detector, to account for detector-to-detector variations in PMT gain. A typical fitted spectrum is shown in Fig. 2.

The pion yield fraction was calculated as

$$f_\pi^i = \frac{Y_\pi^{\rm sim}}{Y_\pi^{\rm sim} + Y_e^{\rm sim}}, \tag{3}$$

where i is the detector number, $Y_\pi^{\rm sim}$ is the total simulated light yield from pions, and $Y_e^{\rm sim}$ is the total simulated light yield from electrons.

In Figure 3, the fitted pion fractions for six of the eight main detectors are shown. The blocked detector MD7 was not included in this analysis, because it required a different approach to determine its pion yield fraction (see

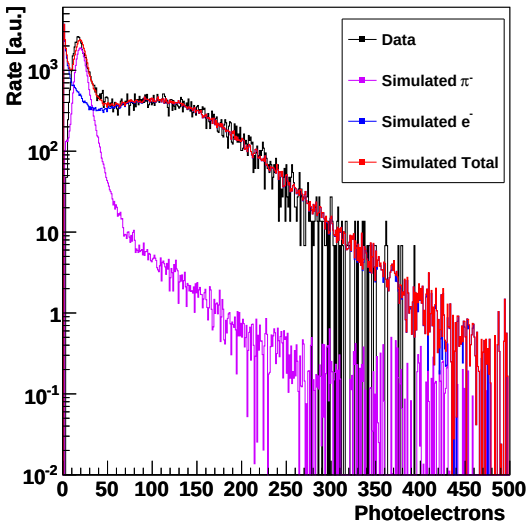

FIG. 2. Typical fit to the photoelectron spectrum from an unblocked main detector (MD4). The black histogram is the data, and the simulated spectra from pions (magenta), electrons (blue) and the sum of the electrons and pions (red) are superimposed.

next subsection). Main detector 3 was also not included, due to a light leak in one of the PMTs that distorted the pulse height spectrum in Event Mode data. The Integrating Mode asymmetry data were taken at a rate six orders of magnitude higher, and so this light leak was negligible compared to the signal in that case. Thus MD3 was included in the asymmetry analysis (Sect. III).

There was a significantly larger detector-to-detector variation in the pion fraction values than what one would expect from statistical uncertainty alone, presumably due to an unaccounted-for systematic effect (we do not know of a physics reason for such a variation). The root-mean-squared deviation (RMS) of the six f_π^i was used as a conservative uncertainty on the average pion yield fraction to account for this systematic effect, giving a detector-averaged value of $f_\pi^{\rm avg} = 0.096 \pm 0.029$ for the unblocked detectors.

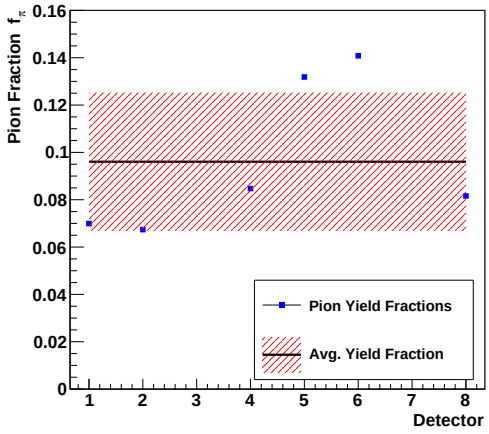

FIG. 3. The fraction of the detector yield due to pions, f_π^i, is shown for each main detector, except MD3 and MD7 (see text). The statistical uncertainties from the fitting routine are smaller than the plotting symbols. Also shown is the average value (black line) and the RMS (hatched area), which we adopt as the uncertainty on the average.

2. Pion yield fraction in MD7

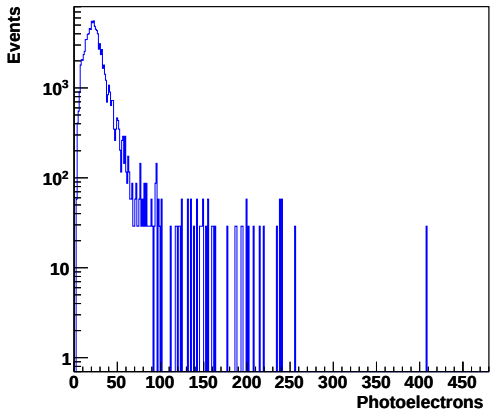

FIG. 4. Photoelectron spectrum from the blocked main detector (MD7). Only the peak due to pions (≈ 20 photoelectrons) is visible; *c.f.* Fig. 1.

The method described above could not be used to determine the pion yield fraction in MD7, the blocked detector, as the fraction of electrons surviving the Pb wall was so small (see Fig. 4) that the electron peak could not be reliably distinguished from the tail of the pion peak in the pulse-height spectrum.

Instead, the assumption was made that both the electrons and the pions were produced with approximate azimuthal symmetry, and so the same pion/electron flux ratio was incident on all 8 detectors. Additional GEANT4 simulations were generated for electrons and pions, of appropriate momenta, incident on the Pb wall in MD7, to determine the signal attenuation factors in the Pb for the electrons and pions, respectively. Applying these attenuation factors to the incident flux ratio extracted from the unblocked octants yielded a pion fraction for MD7 of $f_\pi^7 = 0.81 \pm 0.05$.

3. Neutral yield fraction

The Event Mode data were also used to determine the fraction of the main detector signal which arose due to neutral particles (primarily low-energy gamma rays, but also neutrons). During this data-taking, incident charged particles could be vetoed using the plastic "trigger" scintillators from the tracking system (for a detailed description of the tracking system, see Ref. [35]). These scintillators (218 cm long, 30 cm wide and 1.0 cm thick), when rotated into measurement position, were located just upstream of the main detectors, and covered the entire acceptance of the main detectors for particles from the target passing through the spectrometer. For the measurement of the neutral yield fraction, the data acquisition was triggered by the main detector signal, and charged events were rejected in offline data analysis by placing cuts on the time and pulse-height spectra from the scintillators. The fraction of the yield in the unblocked main detectors that was due to neutral particles was measured to be $(7.8 \pm 0.4)\%$. This was considerably larger than the $< 0.3\%$ fraction observed in the weak charge measurement [20]. This large neutral fraction was due to several effects: (i) the contribution of "punch-through" events, in which $\sim$3 GeV elastically scattered electrons showered in the detector-hut shield wall, (ii) the much lower rate of inelastic electrons at the present kinematics compared to the dominant elastic electrons of the weak charge measurement, and (iii) interactions of beam electrons scattered from the target at very small angles, which could interact in the beampipe downstream of the target, in the vicinity of the detectors, causing a "glow" of low-energy gamma rays.

The effect of the punch-through events on the asymmetry measurement was corrected for separately (see Sec.III D 3), so here GEANT4 simulation was used to estimate the contribution of punch-through events to the neutral yield fraction; subtracting this gives a non-punch-through neutral fraction of $f_{\rm NB}^{\rm UN} = (6.3 \pm 0.6)\%$. As these events are understood to arise mainly due to small-angle events, *i.e.*, events at very low Q^2, they carry essentially no physics asymmetry (parity-violating asymmetries generically scale with Q^2), and we therefore treat this as a pure "dilution" to the asymmetry measurement. They do carry a false asymmetry, $A_{\rm BB}$, the correction for which is described in Sec. III B.

In the case of MD7, however, the presence of the Pb wall upstream of the detector prevented the tracking system

from being rotated in place to veto charged particles. Therefore a direct measurement of the neutral yield fraction for this detector, $f_{\rm NB}^7$, was not possible. Instead, an indirect method was used to infer its value. The assumption was made that the rate of the neutral events was azimuthally symmetric (*i.e.*, that each of main detector, including MD7, experienced the same neutral particle yield). The neutral fraction in MD7 was then larger relative to the unblocked detectors due to the suppression of the charged particle yields (electrons and pions) in the Pb wall. Again, using GEANT4 simulations to determine the suppression factors for electrons and pions due to the wall, the resulting neutral fraction was found to be $f_{\rm NB}^7 = (51 \pm 9)\%$. Further details on the neutral background extraction can be found in Ref. [38].

B. Asymmetry determination

For Integrating Mode data, the raw asymmetry as measured by a given detector was calculated, for every helicity quartet, using:

$$A_{\rm raw} = \frac{Y_+ - Y_-}{Y_+ + Y_-} \tag{4}$$

where $Y_\pm = S_\pm / I_\pm$ is the detector yield, defined as the integrated signal from a given detector $S_\pm$, after subtraction of the electronic pedestal, normalized to the beam current $I_\pm$ in each helicity window. In Eq. 4, $Y_\pm$ is averaged over the two positive (negative) helicity windows in a quartet.

The raw asymmetries $A_{\rm raw}$ were then corrected for several sources of false asymmetry. These included (i) false asymmetries arising from helicity-correlated fluctuations in the properties (trajectory and energy) of the electron beam, $A_{\rm beam}$, (ii) asymmetries arising from interactions of the electron beam with a collimator in the beamline, which we refer to as the beamline background, $A_{\rm BB}$, and (iii) asymmetries caused by re-scattering in the pre-radiators upstream of each detector, which we refer to as the re-scattering bias, $A_{\rm bias}$. Each of these are discussed in turn below.

(i) $A_{\rm beam}$: The helicity-correlated beam correction was determined via

$$A_{\rm beam} = -\sum_{i=1}^{5} \left(\frac{\partial A}{\partial \chi_i} \right) \Delta\chi_i. \tag{5}$$

where $\Delta\chi_i$ are the helicity-correlated differences in the trajectory or energy, as measured over a helicity quartet. The sensitivities $\partial A / \partial \chi_i$ were determined during 6 minute intervals, using linear least-squares regression of the natural fluctuations of the five beam properties: position and angle in x and y, and energy. These corrections were applied to the data for each detector, for each helicity quartet. The net result of these corrections for each detector was small, typically < 0.05 ppm, as detailed in Table I and Table II , and the statistical uncertainty on these corrections was negligible.

(ii) $A_{\rm BB}$: In the weak charge measurement [20], it was found that a false asymmetry arose due to secondary events scattered from the beamline and beam collimator. Such events were determined to be predominantly comprised of low-energy neutral particles which contributed a small amount to the detector signal, but which carried a significant asymmetry, associated with helicity-dependent intensity and/or position fluctuations in the halo around the main accelerated electron beam. This asymmetry could be monitored and corrected for using the asymmetries measured in various auxillary "background" detectors (see Refs. [20], [40] for details). The same technique was adopted in the present analysis, resulting in only a small correction, consistent with zero: $A_{\rm BB} = -0.012 \pm 0.027$ ppm [38].

(iii) $A_{\rm bias}$: After the polarized electrons scattered from the target, they traveled through the spectrometer's magnetic field, causing their spins to precess. In the weak charge measurement [20], this resulted in the initially longitudinally polarized electrons developing a significant transverse (radial) component upon reaching the main detector array. These electrons showered and underwent multiple scattering in the Pb pre-radiators in front of the main detectors. The parity-conserving left-right analyzing power in the low-energy Mott scattering of the electrons from the Pb nuclei caused the asymmetries measured in the two PMTs mounted on either end of a given main detector to differ. In the weak charge measurement, the difference between the asymmetries for the two PMTs was found to be of the order of $A_{\rm diff} = 0.3$ ppm. Fortunately, for perfect detector symmetry, this parity-conserving effect cancels when forming the parity-violating asymmetry of interest. Small symmetry-breaking imperfections in the main detector's geometry and optical response functions lead to a modest correction to the parity-violating asymmetry, which we refer to as the re-scattering bias $A_{\rm bias}$. This effect was extensively studied for the weak charge measurement [20], where the correction

was found to be $A_{\rm bias} = 0.0043 \pm 0.0030$ ppm. The re-scattering effect was also found in the present data set; the difference of the asymmetries from the two PMTs, averaged over all 8 detectors was $A_{\rm diff} = 1.3 \pm 0.3$ ppm. The larger physics asymmetries, and larger statistical uncertainties for the present measurement meant that a similarly detailed study of $A_{\rm bias}$ was not required here. Instead, the previous value of $A_{\rm bias}$ was simply scaled by the ratio of the $A_{\rm diff}$ values between the present measurement and that from the weak charge measurement, and, to be conservative, the uncertainty on $A_{\rm bias}$ was doubled, to yield $A_{\rm bias} = 0.019 \pm 0.028$ ppm, which is small compared to $A^{ii}_{\rm raw}$ (see Ref. [38] for details).

The raw asymmetries were corrected for the false asymmetries discussed above in order to generate the measured asymmetries $A^{ij}_{\rm meas}$ using

$$A^{ij}_{\rm meas} = A^{ij}_{\rm raw} + A_{\rm BB} + A_{\rm bias} + A^{ij}_{\rm beam}. \tag{6}$$

Here the index $i = 1, 2...8$ represents the main detector number, and j represents the data set, either production or transverse. The same corrections $A_{\rm BB}$ and $A_{\rm bias}$ were used for all 8 detectors. With eight main detectors and two data sets (production and transverse), there were sixteen total measured asymmetries $A^{ij}_{\rm meas}$. The raw and measured asymmetries for the production data set are tabulated in Table I, and for the transverse data set in Table II.

A valuable test to ensure that false asymmetries have been properly accounted for is the behavior of the asymmetries under the "slow" reversal, wherein an insertable half-wave plate is periodically inserted into the path of the laser beam in the electron-beam source. This reverses the actual electron beam helicity with respect to the helicity signal from source, and so should simply switch the sign of the measured asymmetry. A failure of this reversal would reveal the presence of several classes of imperfectly corrected-for false asymmetries.

The measured asymmetries were well-behaved under the slow reversal process. For example, Fig. 5 shows the average asymmetry from the 7 unblocked octants plotted *vs.* data subset, where each data subset corresponds to a particular state of the insertable half-wave plate. The measured asymmetry reverses sign as expected; the χ^2 per degree of freedom of a fit of the sign-corrected asymmetries to a single value is an acceptable 0.238.

TABLE I. Asymmetries for each main detector from the production data set. Raw asymmetries, $A_{\rm raw}$, as well as the asymmetries after correction for helicity-correlated fluctuations in beam properties, $A_{\rm raw} + A_{\rm beam}$, are shown. Note that all corrections were less than 0.20 ppm and they caused no appreciable increase in uncertainty.

Main Detector	$A_{\rm raw}$ (ppm)	$A_{\rm raw} + A_{\rm beam}$ (ppm)
1	-2.28 ± 0.57	-2.24 ± 0.57
2	-2.24 ± 0.57	-2.24 ± 0.57
3	-3.17 ± 0.56	-3.19 ± 0.56
4	-2.54 ± 0.58	-2.58 ± 0.58
5	-2.11 ± 0.58	-2.10 ± 0.58
6	0.35 ± 0.58	0.16 ± 0.58
7	1.07 ± 0.95	1.07 ± 0.95
8	-1.46 ± 0.57	-1.49 ± 0.57

TABLE II. Asymmetries for each main detector from the transverse data set. Raw asymmetries, $A_{\rm raw}$, as well as the asymmetries after correction for helicity-correlated fluctuations in beam properties, $A_{\rm raw} + A_{\rm beam}$, are shown. Note that all corrections were less than 0.15 ppm and they caused no appreciable increase in uncertainty.

Main Detector	$A_{\rm raw}$ (ppm)	$A_{\rm raw} + A_{\rm beam}$ (ppm)
1	2.56 ± 2.86	2.58 ± 2.87
2	6.10 ± 2.85	6.14 ± 2.85
3	6.61 ± 2.80	6.58 ± 2.80
4	2.77 ± 2.88	2.72 ± 2.88
5	-4.56 ± 2.90	-4.50 ± 2.90
6	-1.07 ± 2.88	-1.20 ± 2.88
7	18.57 ± 4.64	18.61 ± 4.64
8	-3.87 ± 2.85	-4.00 ± 2.86

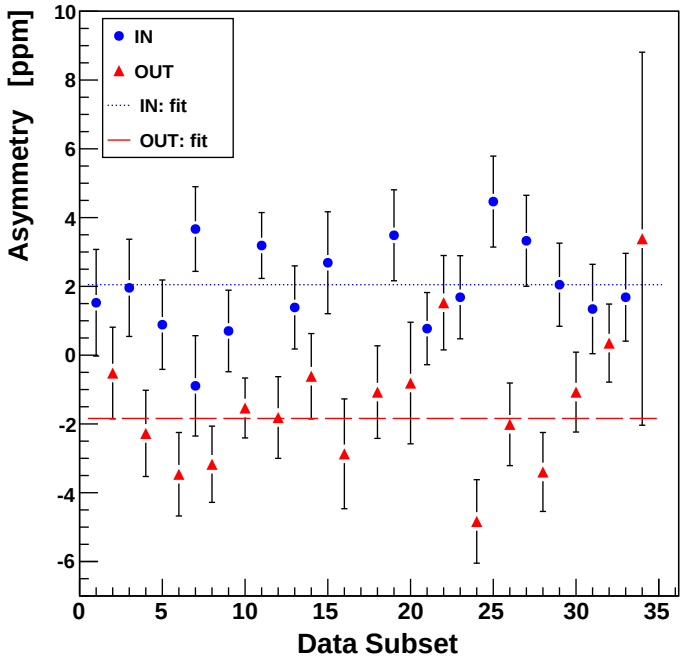

FIG. 5. Measured asymmetry from the production data set, averaged over the unblocked octants, *vs.* data subset, where each data subset corresponds to a particular state of the insertable half-wave plate used to reverse the sign of the electron beam helicity. Each data subset represents roughly 4 hours of data-taking. The "OUT" subsets reveal the unreversed sign of the asymmetry.

C. Extraction of Longitudinal Electron Asymmetry

The measured asymmetries $A^{ij}_{\rm meas}$ include contributions from both scattered electrons and from pions generated in the target. For each particle type, the asymmetry includes parity-violating contributions due to the longitudinal component of the beam polarization, and parity-conserving contributions due to the transverse component of the beam polarization. These latter asymmetries, which are predominantly caused by two-photon exchange processes, vary in a sinusoidal manner with the azimuthal location of the detectors. Finally, each detector's asymmetry was diluted by the fraction of the yield arising from particles other than electrons and pions, which we designate as a neutral background, as it was dominated by low-energy gamma rays.

Thus, the measured asymmetries were parameterized as

$$A^{ij}_{\rm meas} = (1 - f^i_{\rm NB})\Big[(1 - f_\pi^{\rm avg/7})(A^L_e \cos\theta^j_P + A^T_e \sin\theta^j_P \sin\phi^i) + f_\pi^{\rm avg/7}(A^L_\pi \cos\theta^j_P + A^T_\pi \sin\theta^j_P \sin\phi^i)\Big]. \quad (7)$$

The fractional yield from pions seen in MD7 is represented by f^7_π. The average fractional yield seen by the seven unblocked main detectors is $f^{\rm avg}_\pi$. The longitudinal asymmetry from electrons(pions) is $A^L_{e(\pi)}$. The transverse asymmetry from electrons(pions) is $A^T_{e(\pi)}$. The beam polarization angle of data set j is θ^j_P, with $j =$ "prod" (production) or "trans" (transverse). The neutral background yield fraction for MDi is $f^i_{\rm NB}$. The fixed angles corresponding to the azimuthal angle placement of the main detectors are ϕ^i, with $\phi^1 = 0°, \phi^2 = 45°$, etc.

In order to extract the four component asymmetries, A^L_e, A^T_e, A^L_π, and A^T_π, and their uncertainties from the measured asymmetries in Eq. 7, a 'Many-Worlds' Monte-Carlo minimization approach was implemented. The input quantities to this minimization were $A^{ij}_{\rm meas}$ (see Tab. I), $f^{\rm avg}_\pi$ (see Sec. III A 1), f^7_π (see Sec. III A 2), $f^i_{\rm NB}$ (see Sec. III A 3) and θ^j_P. A value for each input quantity was randomly selected from a Gaussian distribution about its mean with a width equal to its uncertainty. These random values were then used to calculate the asymmetry in each MD and for each polarization configuration via

$$A^{ij}_{\rm calc} = (1-\tilde{f}^i_{NB})\Big[(1-\tilde{f}^{\rm avg/7}_{\pi})(A^L_e\cos\tilde{\theta}^j_P + A^T_e\sin\tilde{\theta}^j_P\sin\phi^i) + \tilde{f}^{\rm avg/7}_{\pi}(A^L_\pi\cos\tilde{\theta}^j_P + A^T_\pi\sin\tilde{\theta}^j_P\sin\phi^i)\Big], \tag{8}$$

where a '$\sim$' over a quantity indicates a randomly selected value for that quantity. The function δ, where

$$\delta^2 = \sum(\tilde{A}^{ij}_{\rm meas} - A^{ij}_{\rm calc})^2, \tag{9}$$

was then minimized with respect to the four unknown component asymmetries. This resulted in one possible set of values for each component asymmetry, A^L_e, A^T_e, A^L_π, and A^T_π. The randomization and minimization process was repeated 10^6 times, giving 10^6 extracted values for each of the four component asymmetries and 10^6 values for the calculated asymmetries (shown in Fig. 6). Iterating 10^6 times ensured that each input quantity was sampled sufficiently to span its full probability distribution. This large amount of repeated input sampling also ensured that the distributions of the extracted component asymmetries varied smoothly.

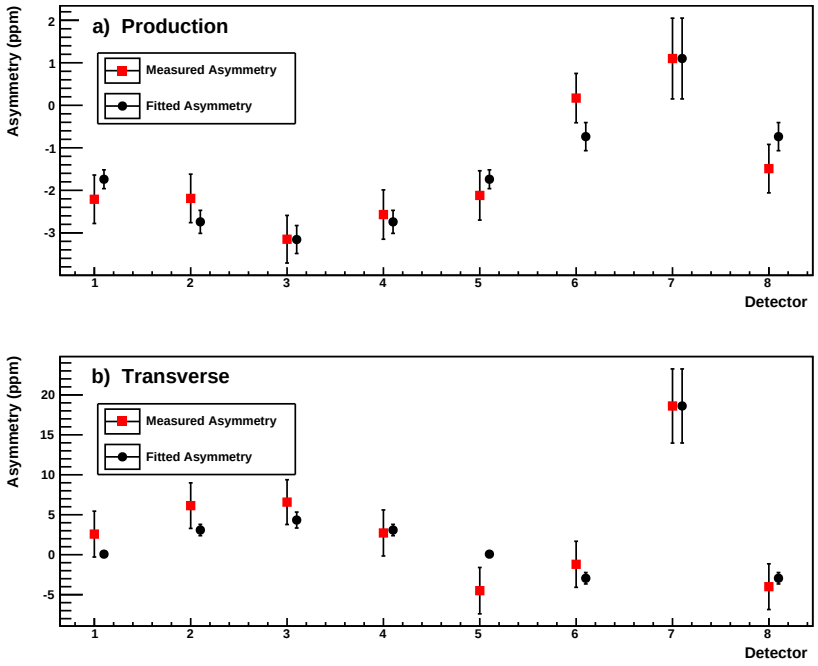

FIG. 6. Measured and fitted asymmetries *vs.* detector number, for both (a) the production data set and (b) the transverse data set.

The root-mean-squared (RMS) deviations of the resulting distributions are taken as their uncertainties. Correlations in the uncertainties of the extracted quantities due to the fitting are automatically accounted for in this 'Many-Worlds' approach. The results for the four component asymmetries and their uncertainties are listed in Table III.

TABLE III. Asymmetries extracted from the 'Many-Worlds' Monte-Carlo minimization process.

Asymmetry	Mean(ppm)	RMS(ppm)
A^L_e	-4.57	1.30
A^T_e	10.7	3.1
A^L_π	22.1	7.8
A^T_π	-52.3	16.8

D. Isolation of Parity-Violating Inelastic Asymmetry

The asymmetry of interest $A_{\rm inel}$ was contained within the longitudinal electron asymmetry, A_e^L, which was determined as described in the previous section. However A_e^L needs to be corrected for several physics backgrounds, and for fact that the beam was not 100% polarized. There were three significant such background processes: (i) events generated by scattering in the aluminum entrance and exit windows of the target, (ii) electrons elastically scattered from the hydrogen that were radiated into the acceptance and (iii) electrons elastically scattered from the hydrogen that were unradiated, but that generated signals in the detectors by "punching through" the concrete walls of the main detector shielding hut.

In order to correct for each of these backgrounds one needs to determine the background fraction f_k, *i.e.*, the fraction of the signal due to background k, as well as the asymmetry due to that background, A_k. Below we discuss each of these backgrounds in turn.

1. Aluminum background

The fractional light-yield contribution from the aluminum target windows, $f_{\rm Al}$, was estimated using GEANT4 simulation, yielding

$$f_{\rm Al} = \frac{Y_{\rm Al}}{Y_{\rm Tot}} = 0.0075 \pm 0.0009 \tag{10}$$

where $Y_{\rm Al}$ is the yield of electrons scattered from the aluminum windows and $Y_{\rm Tot}$ is the total electron yield from the cryogenic target. The cross section parameterizations used in the simulation were taken from Refs. [41, 42]. The longitudinal parity-violating asymmetry from aluminum $A_{\rm Al}^{\rm meas}$ was measured from dedicated runs taken on the aluminum alloy target at the same nea energy. Consistent results for this asymmetry were measured for all 8 detectors (see Fig. 7); the average value was $A_{\rm Al}^{\rm meas} = -3.1 \pm 2.2$ ppm. Correcting for the beam polarization gives $A_{\rm Al} = A_{\rm Al}^{\rm meas}/(P\cos\theta_P^{\rm prod}) = -3.8 \pm 2.7$ ppm.

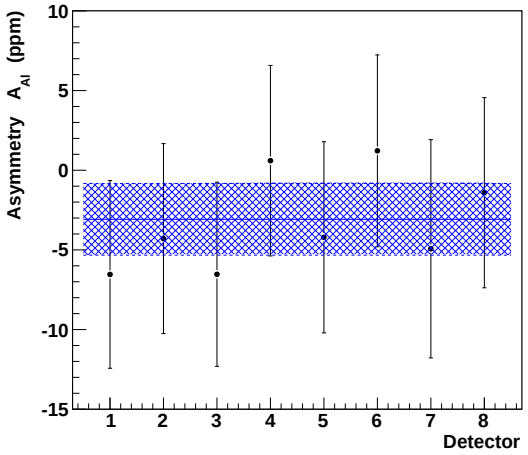

FIG. 7. $A_{\rm Al}$, the asymmetry measured from the aluminum alloy target, plotted *vs.* detector number. The horizontal solid line and hatched region represent the average value and its uncertainty, respectively.

This asymmetry, for the unblocked octants, contains contributions from both electrons scattering from the aluminum as well as pions produced in the aluminum. In principle, the pion and electron asymmetries from aluminum could be separated by comparing the results for the unblocked (electron-dominated) and blocked (pion-dominated) detectors. However, there was not sufficient statistical precision in the aluminum target data to perform such a separation; the measured blocked detector (MD7) asymmetry was identical within errors with that from the unblocked detectors (see Fig. 4). Consequently, we conservatively adopted the 8-detector average with a doubled uncertainty, $A_{\rm Al} = -3.8 \pm 5.4$ ppm as our electron asymmetry from the Al windows.

2. Elastic Radiative Tail

Elastically scattered electrons from the target, if unradiated, were too energetic to make it cleanly into the acceptance of the spectrometer. However, if they underwent hard bremsstrahlung, either before or after the scattering vertex, they could emerge with energies ($\sim$1.0 – 1.2 GeV) that allowed them into the acceptance.

The asymmetry of that fraction of the elastic radiative tail that made it into the acceptance and generated signals in the main detectors was determined using a GEANT4 simulation. Elastic scattered electrons were generated and propagated through the target and the spectrometer; the asymmetries were generated using the standard model value for the weak charge of the proton (which is consistent with our measured value [20]), and the appropriate kinematics. External bremsstrahlung processes were simulated using GEANT4 routines, and internal bremsstrahlung was accounted for following the prescription of Schwinger [43]. The acceptance-averaged asymmetry extracted from the simulation was $A_{\rm El} = -0.58 \pm 0.02$ ppm.

To calculate the background fraction $f_{\rm El}$ for this process, one needs to know cross sections for highly radiated elastic scattering, but also those for the inelastic scattering processes which represent our signal of interest.

For radiative processes, following Mo and Tsai [44] and Tsai [45], the angle-peaking approximation was used when calculating the angular integration of the cross sections, and the equivalent-radiator approximation was used to calculate the internal bremsstrahlung corrections. A Coulomb-correction was included following Aste *et al.* [46]. For inelastic scattering, the cross-section parameterization of Christy and Bosted [41] was adopted. The calculations of the necessary radiative corrections to the cross sections were too computationally expensive to directly embed in the GEANT4 simulation. Instead, the cross sections were calculated using an external piece of computer code originally developed by S. Dasu [47], and modified by a number of authors. These calculated cross sections were used to weight GEANT4 simulated events, which thereby accounted for the experimental acceptance. The resulting elastic radiative tail yield fraction was $f_{\rm El} = Y_{\rm El}/Y_{\rm Tot} = 0.616 \pm 0.036$, where $Y_{\rm El}$ is the yield of elastically scattered electrons.

3. Elastic punch-through

The detector hut shield-wall was designed for the primary weak charge measurement which had a maximum energy of scattered electrons $E' < 1.16$ GeV. For the present measurement, with the beam energy tripled to 3.3 GeV, the E' for elastic scattering events could range up near 3.3 GeV, and thus the concrete shield wall was not thick enough to always absorb all of the energy for the most energetic of these events. An additional background arose from those events which showered in the shield wall, when some of the secondaries in the shower "punched through" and deposited light in the main detectors.

To correct for this, GEANT4 was used to simulate elastically scattered electrons with scattered energies ranging from 150 MeV up to 3.35 GeV. Fig. 8 shows the energy spectrum of scattered electrons for events for which light was deposited in one of the the main detectors. The yield fraction for these punch-through events obtained from the simulation was $f_{\rm PT} = Y_{\rm PT}/Y_{\rm Tot} = 0.0220 \pm 0.0007$, where $Y_{\rm PT}$ is the yield of these punch-through events, and their asymmetry was $A_{\rm PT} = -3.96 \pm 0.04$ ppm.

E. Central Kinematics

A direct measurement of the central value of the four-momentum transfer for the inelastic events, $Q^2_{\rm inel}$, using the tracking system was not possible, because the inelastic events could not be distinguished experimentally from the events in the elastic radiative tail. However, a value for $Q^2_{\rm total}$, the Q^2 for the predicted mixture of inelastic and radiative tail events, was extracted from the GEANT4 simulation. This simulated value, $Q^2_{\rm total(sim)} = 0.0787$ GeV^2 was in reasonable agreement with the experimental value from the tracking system, $Q^2_{\rm total(expt)} = 0.0762$ GeV^2, and the discrepancy between the two was used to estimate the uncertainties on $Q^2_{\rm inel}$ and W. The resulting four-momentum transfer was $Q^2_{\rm inel} = 0.082 \pm 0.002$ GeV^2, and the invariant mass $W = 2.23 \pm 0.06$ GeV.

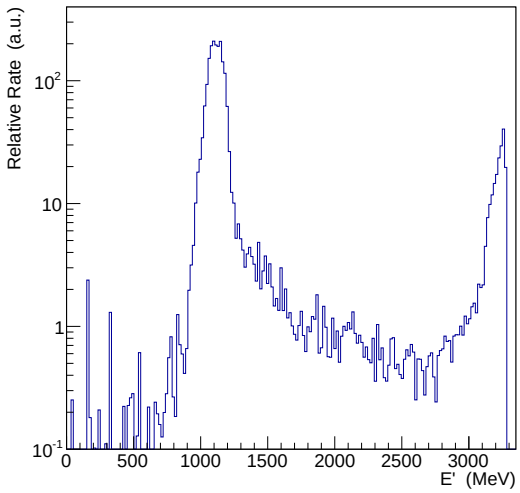

FIG. 8. Simulated energy E' spectrum for elastically-scattered electrons for those events that generated signals in the main detectors (log scale). Note the two distinct peaks. The peak near 1100 MeV represents highly-radiated scattered electrons that pass through the collimators and the apertures of the concrete shield-hut, to directly impinge on the main detector. The peak at the right is due to elastically scattered "punch-through" electrons (see text) which had radiated little energy, but which struck the shield-hut wall, creating a shower that generated signal in the main detectors.

IV. RESULTS

With all backgrounds having been measured or simulated, the final parity-violating asymmetry from inelastic electron-proton scattering $A_{\rm inel}$ was extracted from A_e^L using

$$A_{\rm inel} = \frac{A_e^L/P - \sum_k f_k A_k}{1 - \sum_k f_k}, \tag{11}$$

where $P = (87.0 \pm 0.6)\%$ is the total polarization of the electron beam and $k = [{\rm El}, {\rm PT}, {\rm Al}]$, corresponding to the elastic radiative tail, elastic punch-through, and aluminum backgrounds, respectively.

This physics asymmetry was determined to be

$$\begin{aligned} A_{\rm inel} &= -13.5 \pm 2.0({\rm stat.}) \pm 3.9({\rm syst.})\ {\rm ppm} \\ &= -13.5 \pm 4.4\ {\rm ppm} \end{aligned} \tag{12}$$

at $Q^2 = 0.082\ {\rm GeV}^2$ and $W = 2.23$ GeV.

The uncertainty of the final $A_{\rm inel}$ was dominated by systematic uncertainties (28.7% relative) (see Tab. IV). The four primary contributors, in decreasing order of size, were the pion yield fractions f_π, the neutral background in MD7 $f^7_{\rm NB}$, the elastic radiative tail yield fraction $f_{\rm El}$, and the polarization angles of the electron beam θ_P.

The present result for $A_{\rm inel}$ is compared to the predictions from the AJM group [30] and from Gorchtein *et al.* [26]) in Fig. 9. Our central value is larger than that predicted by either of the two calculations, however it agrees with both within 1.4σ (experimental uncertainty). The relatively limited precision of the present result does not allow us to comment on the appropriateness of the somewhat smaller theoretical uncertainty quoted by the AJM group (compared to that obtained by Gorchtein *et al.*). Nonetheless, the agreement with both calculations lends confidence in the modeling of the $F_1^{\gamma Z}$ and $F_2^{\gamma Z}$ interference structure functions used in these calculations, which are so critical to the $\Box_{\gamma Z}$ contribution to parity-violating electron scattering.

A. Implications of other measured asymmetries

In addition to the inelastic parity-violating asymmetry for electrons, $A_{\rm inel}$, which was the primary motivation for this measurement, three other asymmetries were obtained from fitting the data (see Table III). These were the parity-

TABLE IV. Summary of contributions to $A_{\rm inel}$, and their contributions to the uncertainty $A_{\rm inel}$, in relative percent.

Quantity	Quantity	Value	Contribution to $(\frac{dA_{\rm inel}}{A_{\rm inel}})$
Pion Yield Fraction	$f_\pi^{\rm avg}$	0.096 ± 0.029	21.9%
	f_π^7	0.81 ± 0.05	
Neutral Background in MD7	$f_{\rm NB}^7$	0.51 ± 0.09	12.4%
Elastic Radiative Tail Yield Fraction	$f_{\rm El}$	0.62 ± 0.04	9.8%
Polarization Angle	$\theta_P^{\rm prod}$	$-19.7^\circ \pm 1.9^\circ$	9.3%
	$\theta_P^{\rm trans}$	$92.2^\circ \pm 1.9^\circ$	
Neutral Background in Unblocked MDs	$f_{\rm NB}^{\rm UN}$	0.063 ± 0.006	1.4%
Aluminum Window Asymmetry	$A_{\rm Al}$	-3.8 ± 5.4 ppm	1.0%
Beam Polarization	P	87.0 ± 0.6%	0.8%
Elastic Radiative Tail Asymmetry	$A_{\rm El}$	-0.58 ± 0.02 ppm	0.3%
Re-scattering Bias Effect	$A_{\rm bias}$	0.019 ± 0.028 ppm	0.2%
Aluminum Window Yield Fraction	$f_{\rm Al}$	0.0075 ± 0.0009	0.2%
Punch-Through Yield Fraction	$f_{\rm PT}$	0.0220 ± 0.0007	< 0.1%
Beamline Background Asymmetry	$A_{\rm BB}$	0.012 ± 0.027 ppm	< 0.1%
Punch-Through Asymmetry	$A_{\rm PT}$	-3.96 ± 0.04 ppm	< 0.1%
Regression Correction		$< 0.20 \pm 0.00$ ppm	< 0.1%
Total Systematics			28.7%
Statistics			15.8%
Total:			32.8%

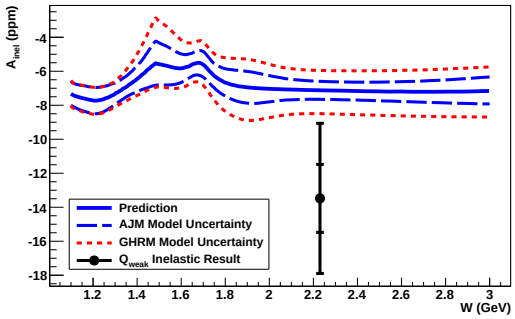

FIG. 9. Model calculations for $A_{\rm inel}$ vs. W, at $Q^2 = 0.08$ GeV^2, and the present measured datum (solid circle). The central values (solid curve) are from the AJM group [30], and the dashed lines represent the theoretical uncertainty from that calculation. The dotted lines are the larger theoretical uncertainties using the approach of Gorchtein *et al.* model [26] (adapted from Fig. 16 of Ref. [30]). The statisical (inner) and total (outer) error bars for the present measurement are indicated.

violating asymmetry for produced pions, A_π^L, and the transverse, or beam-normal single-spin asymmetries (BNSSA) for scattered electrons and produced pions, A_e^T and A_π^T, respectively.

While we did not have sufficient data available to fully correct for the physics backgrounds (elastic radiative tail and aluminum target windows) for these observables, we can nevertheless comment on some implications of these asymmetries.

1. A_e^T

The beam-normal spin asymmetry A_e^T is found to be significant and positive (10.7 ± 3.1 ppm), which is opposite in sign to all such BNSSA measured to date in *elastic* electron scattering experiments [7–11], from the proton and from complex nuclei. The aluminum window contribution to the measured A_e^T must be small, as there is no significant transverse asymmetry seen in our Aluminum dummy-target data (see Fig. 7). In order to correct for transverse asymmetries in the elastic radiative tail, one would need either BNSSA data at the appropriate kinematics, or a reliable theoretical model for the BNSSA in elastic scattering from the proton. The relevant kinematics are (i) that of elastic scattering at 3.3 GeV and $Q^2 \approx 0.21$GeV^2 (for both punch-through events, Sec.III D 3, and events that radiated

after the scattering vertex), and (ii) that of elastic scattering at ≈ 1.1 GeV and $Q^2 \approx 0.05$ GeV^2 (for events that radiated before the scattering vertex). Fortunately, there are data available for the elastic BNSSA from the proton near both these kinematics. Using a 3.0 GeV beam, the G0 forward-angle transverse measurement [9] obtained $A_e^T = -4.1 \pm 1.2$ ppm at $Q^2 = 0.15$ GeV^2, and $A_e^T = -4.8 \pm 2.1$ ppm at $Q^2 = 0.25$ GeV^2. Our own collaboration has a preliminary elastic result of $A_e^T = -5.5$ ppm at 1.16 GeV beam energy and Q^2 = 0.025 GeV^2 (Ref. [48], and to be published). Correcting the measured A_e^T for these asymmetries, weighted by their relative contributions in a manner similar to that outlined in Sec.III D 2, leads to a crude estimate of the purely inelastic A_e^T of $\approx +22$ ppm.

To our knowledge, there is no calculation available to date for the BNSSA for the present inelastic kinematics ($Q^2 = 0.082$ GeV^2 and $W = 2.23$ GeV), which is above the resonance region. However, Carlson *et al.* [49] have investigated the asymmetry for inelastic scattering to the $\Delta(1232)$ resonance, at 1.16 GeV beam energy and forward scattering angle, and predicted large (40 – 50 ppm) positive values. That prediction is in good agreement with a preliminary result at this beam energy from our collaboration (Ref. [50], and to be published). The Carlson *et al.* model included $\Delta(1232)$, $S_{11}(1535)$ and $D_{13}(1520)$ intermediate states in the hadron current. We speculate that the large and positive asymmetry we have observed for inelastic scattering above the resonance region may be driven by a similar mechanism to that explored in the model of Carlson *et al.*

2. A_π^T

The measured transverse asymmetry $A_\pi^T = -52.3 \pm 16.8$ ppm can provide information about the BNSSA in the inclusive production of π^-'s. We did not attempt to correct the measurement for the contribution from pions produced in the aluminum. However, under the assumption that this contribution was small, and thus the signal is dominated by pions produced from the hydrogen, then charge conservation dictates that we are observing multiple mesons in the final state. We are unaware of calculations appropriate to this observable. We note, however, that Buncher and Carlson have calculated the BNSSA in electron scattering in the resonance region when single final-state hadrons are observed [51]. They point out that in the case of inelastic processes in which only an outgoing pion is observed, a BNSSA can arise from a single photon exchange processes, via final-state strong interactions. The generated BNSSA can be of either sign, depending on kinematics [51].

We note that our observation of such large (≈ -50 ppm) BNSSA for inclusive pions at multi-GeV beam energies is important for the design of future precision parity-violation experiments such as the planned 11 GeV MOLLER experiment at Jefferson Lab [52], as misidentified pions might produce significant azimuthally-varying background asymmetries.

3. A_π^L

A large positive asymmetry for parity-violating inclusive π^- production, $A_\pi^L = 22.1 \pm 7.8$ ppm, was extracted from the data. Again, we did not attempt to correct this for pions produced in the aluminum windows so as to extract an asymmetry for production from the proton. We can nevertheless make some comments on this result. The parity-violating asymmetry in real photoproduction should be of the order of the hadronic parity-violation parameter h_π^1, which is experimentally known to be a few 10^{-7} [53]. The asymmetry from electroproduction of the $\Delta(1232)$ from protons or neutrons is negative, as measured by G0 [33]. At much high beam energy (50 GeV), the E158 collaboration observed a negative inclusive pion production asymmetry of order -1 ppm [54].

Explanation of the observed large *positive* asymmetry would seem to require alternative physics mechanisms. One possibility is the electroproduction of polarized hyperons, Λ and Σ. Large ($\sim 50\% - 75\%$) transfer of polarization has been observed in electroproduction of hyperons at similar kinematics [55]. The pion-emitting weak decay (eg $\Lambda \to p\pi^-$) of such hyperons is self-analyzing, and pions emitted forward or backward in the hyperon rest frame may have different kinematic acceptances, thus leading to an asymmetry in their detection efficiency. A similar effect was seen in forward-angle parity-violating electron scattering at 3.0 GeV beam energy by the G0 collaboration [56] who found large, positive asymmetries for protons from hyperon decay.

An alternative hypothesis is that there are large contributions from isoscalar exchange, *i.e.*, the virtual Z^0 producing multipion final states and coupling to the nucleon via isoscalar Reggeon exchange [57]. There is insufficient information in the present data to distinguish between these possibilities.

Again, our observation of large ($\approx +20$ ppm) inclusive parity-violating pion asymmetries is relevant as a source of potential backgrounds for the MOLLER experiment [52].

V. SUMMARY

We have measured the parity-violating asymmetry in the inelastic scattering of electrons from the proton above the resonance region, at $Q^2 = 0.082$ GeV^2 and $W = 2.23$ GeV. The result, $A_{\rm inel} = -13.5 \pm 2.0(\text{stat.}) \pm 3.9(\text{syst.})$ ppm, is in agreement with two dispersion model calculations [30] and [26], and therefore lends confidence in these models as used to calculate the $\Box_{\gamma Z}$ contribution to precision parity-violating electron scattering measurements, and therefore to precision tests of the Standard Model.

We also observed a large positive BNSSA in inelastic electron scattering, a large negative BNSSA in the inclusive production of pions, and a large positive asymmetry in the parity-violating inclusive production of pions.

VI. ACKNOWLEDGMENTS

This work was supported by DOE Contract No. DEAC05-06OR23177, under which Jefferson Science Associates, LLC operates Thomas Jefferson National Accelerator Facility. Construction and operating funding for the experiment was provided through the U.S. Department of Energy (DOE), the Natural Sciences and Engineering Research Council of Canada (NSERC), the Canadian Foundation for Innovation (CFI), and the National Science Foundation (NSF) with university matching contributions from William and Mary, Virginia Tech, George Washington University, and Louisiana Tech University. We thank the staff of Jefferson Lab, in particular the accelerator operations staff, the target and cryogenic groups, the radiation control staff, as well as the Hall C technical staff for their help and support. We are grateful for the contributions of our undergraduate students. We thank TRIUMF for its contributions to the development of the spectrometer and integrating electronics, and BATES for its contributions to the spectrometer and Compton polarimeter. We are indebted to P.G. Blunden, M. Gorchtein, N.L. Hall, W. Melnitchouk, M.J. Ramsey-Musolf, and A.W. Thomas for many useful discussions.

[1] A. J. R. Puckett et al., Phys. Rev. **C96**, 055203 (2017), [erratum: Phys. Rev.C98,no.1,019907(2018)].
[2] A. Afanasev, P. G. Blunden, D. Hasell, and B. A. Raue, Prog. Part. Nucl. Phys. **95**, 245 (2017).
[3] C. E. Carlson and M. Vanderhaeghen, Ann. Rev. Nucl. Part. Sci. **57**, 171 (2007).
[4] O. Koshchii and A. Afanasev, Phys. Rev. **D98**, 056007 (2018).
[5] P. A. M. Guichon and M. Vanderhaeghen, Phys. Rev. Lett. **91**, 142303 (2003).
[6] P. G. Blunden, W. Melnitchouk, and J. A. Tjon, Phys. Rev. Lett. **91**, 142304 (2003).
[7] S. P. Wells et al. (SAMPLE), Phys. Rev. **C63**, 064001 (2001).
[8] F. E. Maas et al., Phys. Rev. Lett. **94**, 082001 (2005).
[9] D. S. Armstrong et al. (G0), Phys. Rev. Lett. **99**, 092301 (2007).
[10] D. Androic et al. (G0), Phys. Rev. Lett. **107**, 022501 (2011).
[11] S. Abrahamyan et al. (HAPPEX, PREX), Phys. Rev. Lett. **109**, 192501 (2012).
[12] D. B. Ríos et al., Phys. Rev. Lett. **119**, 012501 (2017).
[13] A. Esser et al., Phys. Rev. Lett. **121**, 022503 (2018).
[14] I. A. Rachek et al., Phys. Rev. Lett. **114**, 062005 (2015).
[15] Y. W. Zhang et al., Phys. Rev. Lett. **115**, 172502 (2015).
[16] B. S. Henderson et al. (OLYMPUS), Phys. Rev. Lett. **118**, 092501 (2017).
[17] D. Rimal et al. (CLAS), Phys. Rev. **C95**, 065201 (2017).
[18] C.-Y. Seng, M. Gorchtein, H. H. Patel, and M. J. Ramsey-Musolf (2018), arXiv:1807.10197.
[19] C.-Y. Seng and U.-G. Meißner, Phys. Rev. Lett. **122**, 211802 (2019).
[20] D. Androić et al. ($Q_{\rm weak}$ Collaboration), Nature **557**, 207 (2018).
[21] J. Erler, A. Kurylov, and M. J. Ramsey-Musolf, Phys. Rev. **D68**, 016006 (2003).
[22] D. Becker et al., Eur. Phys. J. **A54**, 208 (2018).
[23] M. J. Musolf and B. R. Holstein, Phys. Lett. **B242**, 461 (1990).
[24] M. Gorchtein and C. J. Horowitz, Phys. Rev. Lett. **102**, 091806 (2009).
[25] A. Sibirtsev, P. G. Blunden, W. Melnitchouk, and A. W. Thomas, Phys. Rev. **D82**, 013011 (2010).
[26] M. Gorchtein, C. J. Horowitz, and M. J. Ramsey-Musolf, Phys. Rev. **C84**, 015502 (2011).
[27] B. C. Rislow and C. E. Carlson, Phys. Rev. **D83**, 113007 (2011).
[28] B. C. Rislow and C. E. Carlson, Phys. Rev. **D88**, 013018 (2013).
[29] P. G. Blunden, W. Melnitchouk, and A. W. Thomas, Phys. Rev. Lett. **107**, 081801 (2011).
[30] N. L. Hall, P. G. Blunden, W. Melnitchouk, A. W. Thomas, and R. D. Young, Phys. Rev. **D88**, 013011 (2013).
[31] N. L. Hall, P. G. Blunden, W. Melnitchouk, A. W. Thomas, and R. D. Young, Phys. Lett. **B753**, 221 (2016).
[32] F. D. Aaron et al. (H1), JHEP **09**, 061 (2012).
[33] D. Androic et al. (G0) (2012), arXiv:1212.1637.

[34] D. Wang et al. (Jefferson Lab Hall A), Phys. Rev. Lett. **111**, 082501 (2013).
[35] T. Allison et al. (Q_{weak} Collaboration), Nucl. Instrum. Methods **A781**, 105 (2015).
[36] P. A. Adderley et al., Conf. Proc. **C110328**, 862 (2011).
[37] M. Hauger et al., Nucl. Instrum. Methods **A462**, 382 (2001).
[38] J. F. Dowd, Ph.D. thesis, College of William and Mary (2018).
[39] S. Agostinelli et al. (GEANT4), Nucl. Instrum. Methods **A506**, 250 (2003).
[40] E. Kargiantoulakis, Ph.D. thesis, University of Virginia (2015).
[41] M. E. Christy and P. E. Bosted, Phys. Rev. **C81**, 055213 (2010).
[42] P. E. Bosted and M. E. Christy, Phys. Rev. C **77**, 065206 (2008).
[43] J. Schwinger, Phys. Rev. **A24**, 2353 (1981).
[44] L. W. Mo and Y.-S. Tsai, Rev. Mod. Phys. **41**, 205 (1969).
[45] Y.-S. Tsai, Rev. Mod. Phys. **46**, 815 (1974), [Erratum: Rev. Mod. Phys.49,521(1977)].
[46] A. Aste, C. von Arx, and D. Trautmann, Eur. Phys. J. **A26**, 167 (2005).
[47] S. R. Dasu, Ph.D. thesis, The University of Rochester (1988).
[48] B. P. Waidyawansa (Qweak), AIP Conf. Proc. **1560**, 583 (2013).
[49] C. E. Carlson, B. Pasquini, V. Pauk, and M. Vanderhaeghen, Phys. Rev. **D96**, 113010 (2017).
[50] Nuruzzaman (Qweak), in *Proceedings, CIPANP 2015* (2015), arXiv:1510.00449.
[51] B. Buncher and C. E. Carlson, Phys. Rev. **D93**, 074032 (2016).
[52] J. Benesch et al. (MOLLER) (2014), arXiv:1411.4088.
[53] D. Blyth et al. (NPDGamma), Phys. Rev. Lett. **121**, 242002 (2018).
[54] P. L. Anthony et al. (SLAC E158), Phys. Rev. Lett. **95**, 081601 (2005).
[55] D. S. Carman et al. (CLAS Collaboration), Phys. Rev. C **79**, 065205 (2009).
[56] D. S. Armstrong et al. (G0), Phys. Rev. Lett. **95**, 092001 (2005).
[57] M. Gorchtein, private communication.